4. Volcanic Seismic Sources

Douglas Dreger and Hrvoje Tkalcic

4.1 Long Valley, CA Seismicity

In the spring of 1997 the Long Valley Caldera began a new phase of unrest that lasted through early 1998. This unrest initiated in May with reinvigored inflation of the resurgent dome observed on Long Valley geodetic networks (Langbein et al., 1998). In June the seismicity rate began to increase markedly, the deformation rate continued to be high and the flux of CO_2 release increased between September to December. The seismic unrest culminated on November 22 with a series of four magnitude 4.6-4.9 earthquakes located in the south moat of the caldera. Preliminary moment tensor analysis of these events revealed anomalous seismic radiation. Deviatoric moment tensors have large non-double-couple(NDC) components, and full moment tensor inversions reveal a component of coseismic volumetric expansion in all four events (Figure 10.6). These are the first direct observations of coseismic volumetric expansion in Long Valley seismicity.

The double-couple and full moment tensor inversions have 5 and 7 free parameters respectively. We evaluated whether the full moment tensor solutions provides a significant improvement in fit considering the increase in model parameters using an F-test (e.g. Menke, 1989). The F statistic is formed from the ratio of the two data-model variances. It is possible to compute critical values, F_{crit}, for specific levels of confidence and degrees of freedom in the inversion (e.g. Menke, 1989). If observed F exceed F_{crit} then the improvement in fit is statistically significant at the prescribed level. In our inversions of complete, three-component, long-period (0.02 to 0.05 Hz) displacement waveforms we have 3000 data points for 5 stations (200 points per component with dt=1s). The F-test assumes that each time point is uncorrelated, which is clearly not valid. For example a number of points are required to define the pulse width of the P-wave. We use a 20s period low pass butterworth filter in processing the data and therefore assume that the data is correlated over a 20s time scale. This reduces the number of uncorrelated data to 150 points. The degrees of freedom are then 145 and 143 for the double-couple and full moment tensor inversions, respectively. The F_{crit} for these degrees of freedom and 95% significance level is 1.32. Observed F values for events 1, 2, 3 and 4 are 1.96, 2.06, 3.59, and 2.33 respectively, indicating that the improvement in fit afforded by the full moment tensor parameterization is statistical significant above the 95% level. We note further that even in the extreme case of two uncorrelated points per trace the observed F are statistically significant at the 95% level.

A Jackknife test was performed to investigate the sensitivity of the isotropic components and general orientation of the principle axes of the seismic moment tensors to variations in the input data. This test evaluates whether lateral heterogeneity or whether a single station or groups of stations may be biasing the results. The Jackknife test revealed that the isotropic components for the anomalous events are significantly separated from double-couple reference earthquakes, and that the isotropic components that have been calculated are stable for all combinations of 1-, 2-, 3-, 4- and 5-stations indicating that there is no station specific or propagation path bias.

Figure 10.6 shows that the solutions for the anomalous events have significant isotropic components indicating volumetric expansion at the source. With the exception of EVT1 the deviatoric parts of the moment tensors are primarily CLVDs. The combined isotropic-CLVD solutions and anomalously long source durations apparent in the P-waveforms of these events together with the observation of a compressional strain transient recorded at the Devil's Post Pile borehole strainmeter suggest that fluids were involved in the source process (Dreger et al., 1999). Langbein et al (1998) report that the strain transient and other geodetic data may be modeled as either an inflation source beneath the south moat of the caldera or as right-lateral strike-slip on a west-northwest trending fault, which is consistent with background seismicity. The seismic moment tensor observations and the strain transient suggest that seismicity was triggered by the injection of high pressure fluid or possibly by pressurization of water saturated faults in the south moat by a pressure pulse generated by magmatic heating.

4.2 References

Dreger, D. S., H. Tkalcic, and M. Johnston, Broadband Evidence of Non-Double-Couple Moment Tensors and Volumetric Expansion in Recent Mammoth Lakes, California, Earthquakes, *submitted to Science,* 1999.

Langbein, J., S. Wilkinson, M. Johnston, J. Feinberg, R. Bilham, The 1997-98 Inflation of Long Valley Caldera and comparison with the 1989-95 episode, EOS, 79, 949, 1998.

Menke, W., Geophysical Data Analysis: Discrete Inverse Theory, Academic Press Inc., pp289, 1989.

5. Development of Procedures for the Rapid Estimation of Ground Shaking

Douglas Dreger and Anastasia Kaverina

5.1 Introduction

This project focused on the development of methodology for the near-real-time estimation of earthquake strong ground motion with the objective of providing this information on a regional (statewide) scale. A critical objective of our development was to provide seamless implementation and uniform performance in varied network coverage. To accomplish this goal we: 1) refined a finite fault inverse method to determine fault slip using regional distance stations; 2) developed a strong motion simulation procedure that uses finite source information as input; 3) investigated the incorporation of site type correction factors, 4) and investigated alternative methods to improve the simulation of high frequency strong ground motions. We have successfully completed these tasks and have developed software that calculates model-based estimates of strong shaking that include the focussing effects due to source directivity. The method we have developed estimates PGA, PGV and spectral acceleration at periods of 0.3, 1.0 and 3.0 seconds. These model predictions may be used to interpolate actual strong motion observations (when available) in the same manner as the southern California TriNet ShakeMap (Wald et al. 1999), and we provide examples of data/model shakemaps for the Landers and Northridge earthquakes. These examples show that it is possible to calculate robust shakemaps even in extremely sparse coverage.

5.2 Finite Fault Inversion for Slip Distribution

We extensively tested the algorithms with data recorded for the 1992 Landers and 1994 Northridge earthquakes, and compared our regionally derived fault slip maps with those obtained using local strong motion recordings. Favorable comparisons indicate that our methodology is capable of uniquely determining the causative fault plane of the earthquake, the slip dimension (both along strike and down dip), the earthquake rupture velocity, and a reasonable characterization of the gross slip distribution, suggesting that the derived source parameters may be used to simulate near- source strong ground motions. The code will be integrated into the Rapid Earthquake Data Integration (REDI) system (Gee et al., 1996) operated by the Berkeley Seismological Laboratory. Our preliminary testing indicates that the essential source information may be obtained within 4 to 20 minutes following the determination of a seismic moment tensor solution depending upon the level of approximation required.

5.3 Strong Motion Simulation

The focus of this task was to use the regionally derived fault slip maps to simulate the distribution of near-source strong ground motion, and to compare the model predictions with observations to calibrate the methodology. Additionally, we tested method of hybrid Green's function (Kamae et al., 1998), the composite source (Zeng, 1994) method and empirical attenuation relationship (Somerville et al., 1997) to attempt to better simulate higher frequency ground motions. Our basic method of ground motion simulation is one we developed in which fault slip is deterministically integrated using appropriate local Green's functions. We found that this deterministic approach performed reasonably well in the comparisons of PGV, however the Sa comparisons had mixed results. The PGA, PGV and Sa maps were all found to be successful in outlining the area of observed large ground motions, however there were varying degrees of misfit of the location of predicted and observed maximal values. The methods of Kamae et al. (1998) and Zeng (1994) improved the results somewhat but not to a degree that offsets their higher computational expense. PGA and Sa (0.3, 1.0 and 3.0 seconds) were well modeled using the approach of Somerville et al. (1997), which utilized the regionally derived finite source information as input. The empirical approach is also extremely fast and requires information available after the initial fault plane and rupture velocity inversion, which is also relatively fast. The best shakemaps for the two study events were obtained by taking the larger of the two values from the deterministic and the empirical maps. We call this map our 'conservative shakemap'. The empirical component of the conservative shakemap is found to explain the mean attenuation of the observed strong motions very well and the deterministic component provides a better estimate of the large near-fault ground motions.

5.4 Site Corrections

We explored ways to improve the predicted strong motion parameters by applying site corrections to the synthetic ground motions. Implementation of the empirical site corrections applied to Quaternary, Tertiary and Mesozoic sites (Borcherdt, 1994; Park and Elrick, 1998; Wald, 1999) improved the agreement with the observations but not enough to offset a systematic under prediction at LA basin sites. A second method used two 1D velocity models to characterize rock and soil sites. The application of site specific Green's functions provided a noticeable improvement in the predicted shakemap but stations located within the LA Basin remain underpredicted.

5.5 Generation of a ShakeMap

We have developed a multi-staged algorithm to generate a shakemap. First, line source or course planar inversions are performed to determine the rupture velocity, causative fault plane and slip dimension of an earthquake. This information may then be used to generate a shakemap using an attenuation relationship (e.g. Somerville et al. 1997) sensitive to directivity and site class. If local strong motion data is available it may be integrated with the empirical values to develop a data/model shakemap. With relatively dense coverage the map would be data driven with model predictions contributing only in the regions where there are gaps in coverage. Following the determination of the causative fault plane and rupture velocity, processing may be continued to determine a higher resolution picture of the distribution of fault slip. The higher resolution slip map is then used to simulate near-source synthetic time histories from which values of PGA, PGV and spectral acceleration may be measured. We then combine the larger of the simulated and the empirical ground motions to produce a 'conservative shakemap'. As in the first stage of processing available data may be integrated into the shakemap, where model predictions are used to interpolate only in areas where there are no observations (Figure 10.7). A common multi-parametric attenuation relationship provides seamless transition from one level of approximation to another as more data and model information becomes available.

5.6 Acknowledgments

Many thanks to Arben Pitarka for performing strong motion calculations at our request and to Yuehua Zeng for providing his programs to us.

5.7 References

Borcherdt, R. D., Estimates of site-dependent response spectra for design (methodology and justification), *Earthquake Spectra, 10,* 617-654, 1994.

Zeng, Yuehua, A composite source model for computing realistic synthetic strong ground motions, *Geophys.Res.Lett., 21*, 725-728, 1994.

Gee, L. S., Real-time seismology at UC Berkeley; the Rapid Earthquake Data Integration Project, *Bull. Seism. Soc. Am., 86,* 1037-1106, 1996.

Somerville, P. G., N. Smith, R. Graves and N. Abrahamson, Modification of empirical strong ground motion attenuation relations to include the amplitude and duration effects of rupture directivity, *Seism.Res.Lett., 68,* 199-222, 1997.

Kamae K., Irikura K. and A. Pitarka, A technique for simulating strong ground motion using hybrid Green's function, *Bull. Seism. Soc. Am., 88,* 357-367,1998.

Park, S. and S. Elrick, Predictions of shear-wave velocities in Southern California using surface geology, *Bull. Seism. Soc. Am., 88,* 677-685, 1998.

Wald, D. J., V. Quitoriano, T. H. Heaton, H. Kanamori, C. W. Scrivner and C. B. Worden, TriNet "ShakeMaps": rapid generation of instrumental ground motion and intensity maps for earthquakes in southern California, *Earthquake Spectra, 15*, 537-556, 1999.

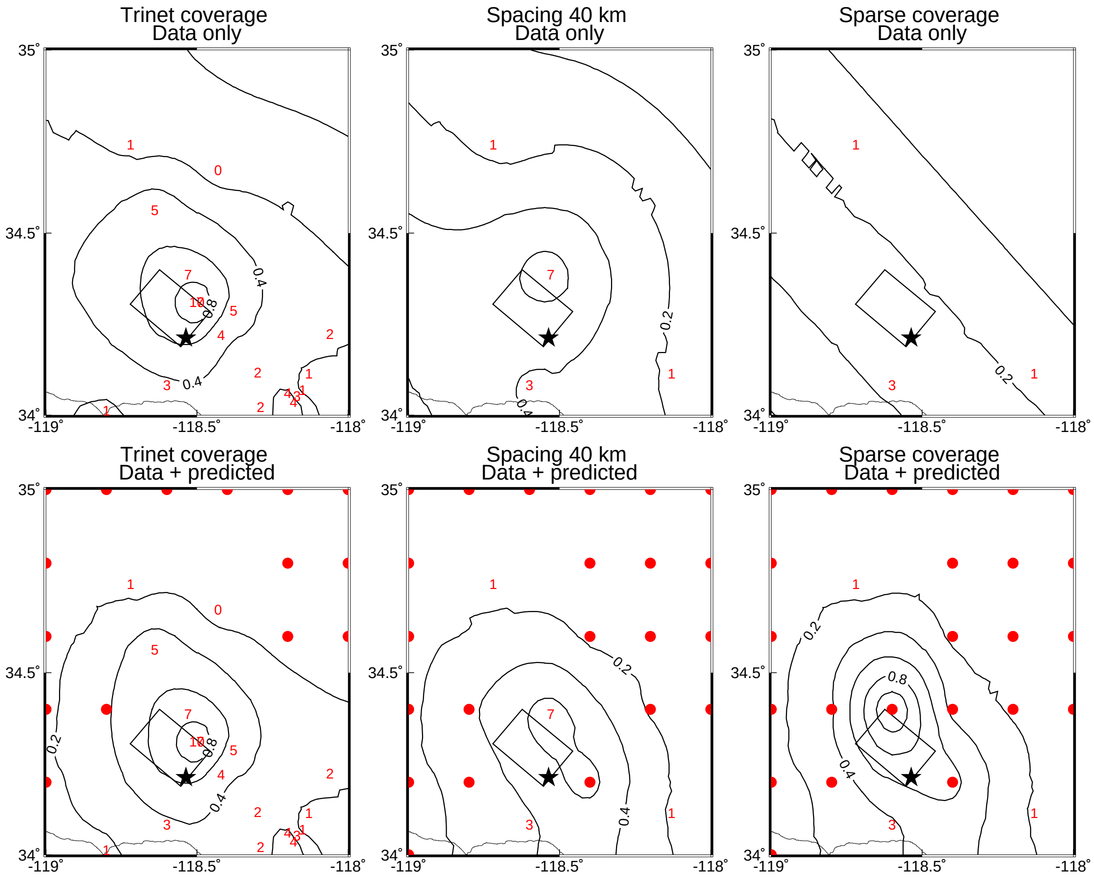

Figure 10.7: Examples of PGA shakemaps for the Northridge 1994 earthquake with different near-source coverage. The upper row shows shakemaps based on the data only: for TriNet stations (left), for 4 stations (center) and for 3 stations only (right). Actual PGA values are indicated in 0.1g in red. Contours of PGA depend strongly on the station coverage. The lower row shows respective PGA shakemaps in which data is augmented by predicted 'conservative' estimates of PGA, shown as red dots. For all cases, the region with large strong motion is well defined and predicts the observed directivity.

6. Parkfield Studies

T. V. McEvilly, R. M. Nadeau, R. W. Clymer, R. A. Uhrhammer,
Collaborating Scientists: L. R. Johnson, C. G. Sammis, W. Foxall, V. Korneev

6.1 Background

A high-resolution seismographic network (HRSN) for the Middle Mountain stretch of the San Andreas fault zone, where the M6 event is presumably nucleating, was installed in boreholes beginning in 1986. In November 1987, the Varian well vertical array was installed and the first VSP survey was conducted, revealing clear S-wave anisotropy in the fault zone. During 1988, the network was completed to ten 3-component 500 sps radio-telemetered stations, incorporating a deep (572 m) sensor in the Varian well string into the network. The Varian system was slaved in 1988, for about two years, to the Vibroseis control signals, allowing simultaneous recording of vibrator signals on both systems. In 1991, low-gain event recorders (from PASSCAL) were installed to extend the dynamic range to M_L about 4.5. In 1991, we determined a local 3-D velocity model by joint inversion, and data reduction methods were designed to handle the massive data sets in a monitoring mode. Since 1989, new analysis techniques gradually have been developed to extract and display the information contained in the high-resolution data from both Vibroseis and microearthquakes to support a variety of research efforts in the project. The daunting technical and data processing requirements for this project were met only through the participation of several graduate students and technical personnel at the Lawrence Berkeley National Laboratory Center for Computational Seismology and Geophysical Measurements Facility. The system has recorded more than 10000 microearthquakes in the Parkfield region along with many times that number of regional and teleseismic events. More than 5000 good quality 3-D locations make up the catalog for the 40 km stretch of the fault zone centered at Middle Mountain. More than 50 controlled-source data sets from the Vibroseis monitoring program have also been gathered from mid-1987 until its termination in 1997.

About two-thirds of all the Parkfield earthquakes are members of a few hundred sequences of as many as 20 or more characteristic events - regularly recurring earthquakes so similar that waveform coherency exceeds 0.98 over a 50Hz+ bandwidth for the entire wavetrain, Figure 10.8. Relative hypocenter locations for these types of events differ only by 5-10 meters, near the resolution of our analysis. This phenomenon may be common to creeping seismogenic fault zones in general, but there are not the high-resolution networks in place to test this at the $-1 < M < 2$ level where recurrence times are less than a few years. This new view of fault-zone process is fundamental to our research program, and we are completing the characterization of the fault zone up to the present time while also extending the characterization of fault seismicity to the entire creeping part of the full San Andreas system. 'Characteristic' implies more than just 'similar', a criterion easily satisfied by nearby events when observed at lower bandwidth. Very narrow moment and recurrence interval distributions are characteristic of the repeating events we are working with, Figure 10.9.

There are immediate consequences of characteristic recurrence. One striking implication follows from the near-constant moment release rate in a sequence. If we can independently estimate the associated slip rate on the fault at the sequence, an entirely new approach to source parameter estimation is possible that is independent of spectral corners, yielding a set of scaling relations among moment, area, slip and stress drop that seem to hold for the range $0 < M < 6$ on the San Andreas fault in central California. An inescapable result is a strong moment dependence for stress drop, with kilobar+ values implied for the small events. There is supporting petrological evidence in exhumed fault zones for these extreme hypocentral conditions.

Systematic changes in recurrence intervals are seen in some sequences, equivalent to changes in moment release rates, implying change in slip rate. The characteristic sequences thus become strain meters within the fault zone, and we have begun to use this idea to map the changing slip rate throughout the fault zone. The results are generally consistent with changes expected to accompany the 10/92-12/94 M4.5+ major earthquake sequences, and there is good correlation of recurrence-derived slip rates with surface-based measurements of deformation.

The highly structured seismicity at Parkfield stands in stark contrast to the much less organized picture of earthquake rupture and fault deformation painted by conventional lower resolution data sets. When high-resolution data are processed using advanced techniques, the appearance of diffuse uncorrelated seismicity largely resolves itself into an organized pattern of repeating

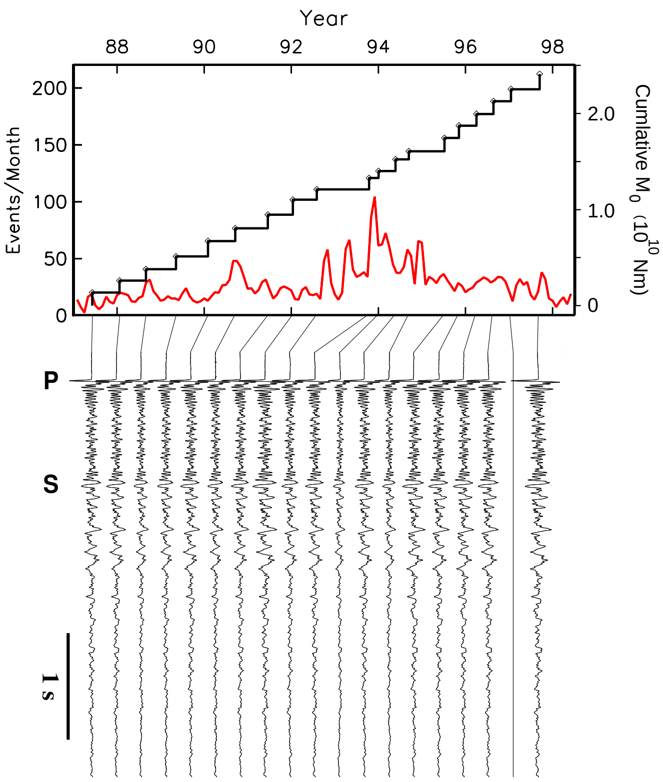

Figure 10.8: Step diagram of seismic moments and recurrence intervals (top) and vertical component seismograms recorded at Parkfield on borehole station VCA (inoperative for event 18) (bottom) for a repeating earthquake sequence containing 19 events. Among events in repeating sequences, seismic moments, waveforms and locations are virtually identical and recurrence times are quasi-periodic.

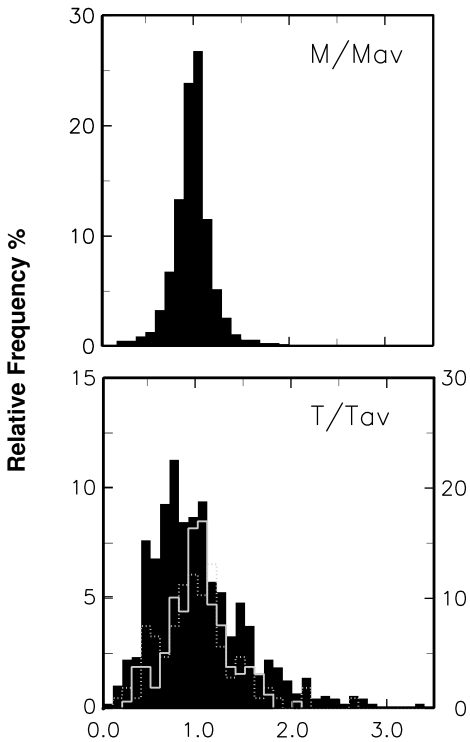

Figure 10.9: Distributions of sequence-normalized seismic moments (top) and recurrence intervals (bottom) for 160 repeating earthquake sequences. Coefficients of variation (COVs) for moments and intervals are 0.22 and 0.49, respectively, for the full data set (filled black bars). COVs for recurrence intervals are 0.42 and 0.32, respectively, for subsets (right scale) of larger (magnitude > 1.0) events (broken line) and events occurring before June 1992 (solid gray line). These distributions characterize the size and recurrence time variability for all 160 repeating sequences and provide the basis for a variety of unique analyses now possible using repeating sequences. These include slip rate estimates at depth, the augmentation and testing of statistically based earthquake recurrence and forecast models, and the estimation and mapping of fault healing rates in nature.

earthquake groups having the same size, location, waveforms and constant recurrence interval. In addition, the hypocenters of most earthquakes become restricted to a narrow planar core of seismic strain release within which the repeating earthquake sites cluster on several scales – clusters of clusters. Fractal analyses of the highly resolved hypocenters show a considerably lower fractal dimension, (D $\sim$ 1), than that observed and predicted for Parkfield based lower resolution data (typically, D = 2 to 3). In addition, the fractal pair-correlation function shows discrete behavior (undulations) indicating a strong heterogeneity in the spatial distribution of earthquakes on the SAF at Parkfield. This discrete behavior is masked, however, by uncertainties in location when less well resolved catalogs such as NCSN are used, Figure 10.10.

At Parkfield, repeating earthquakes comprise a large part of the earthquake population, yet their fraction of the total seismicity is not constant through space and time. Rather, this fraction exhibits systematic variations which appear to be closely related to fault slip and the earthquake process. Some subsections of the fault at Parkfield, for example, show a cyclic pattern of decreasing amplitude in the time evolution of the fraction of repeating earthquakes, Figure 10.11. We have found differences among seismogenic fault segments in central California, apparently related closely to slip rate. For example, this new measure of fault activity varies from about 70% at Parkfield, using the borehole network data base (48% for the same region using NCSN waveforms only) to 13% and 6% respectively for NCSN data on the southern Hayward/Mission and northern Hayward faults. At Parkfield, the fraction, as well as the total seismicity, drops rapidly as the locked part of the fault is approached. We have begun a more intensive investigation of this phenomenon in order to characterize the San Andreas and subsidiary faults from Parkfield to the Bay Area, where we can again tie in the NCSN/borehole performance difference using the developing Hayward Fault Borehole Network. The goal of this proposed effort is to test the utility of the repeating earthquake statistic and the waveform similarity characterizations to help delineate fault properties and fault segment boundaries based more quantitatively on what appears to be a measure of fault slip rate.

We have begun a detailed characterization of waveform similarity with earthquake separation that we have named the 'Cluster Signature' (see figure in the Hayward Fault section) Highly similar repeating earthquakes are co-located to a spatial resolution proportional to the signal bandwidth - about 5-10 m for the 100 Hz borehole

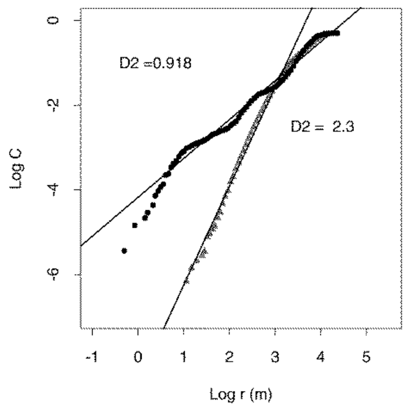

Figure 10.10: 3D two-point correlation sum verses hypocenter separation distance for Parkfield earthquakes recorded on the High Resolution Seismic Network, HRSN (filled circles), and the Northern California Seismic Network, NCSN (open triangles). The slopes of the curves provide estimates of the D2 fractal dimension for the distribution of hypocenters. The discrete fractal behavior and low fractal dimension seen using the HRSN data are masked by large location errors typical of routine high quality catalogues such as the NCSN.

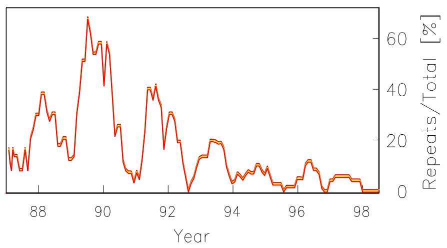

Figure 10.11: Fraction of repeating earthquakes through time for a 14 by 6 km subsegment of the SAF enclosing the nucleation region of the 1966 M6 earthquake at Parkfield. The figure shows that the relative number of repeating to non-repeating events is not constant through time but varies systematically with a 1.5 to 2 year cyclicity and decreasing peak amplitudes occurring subsequent to the late 1992 increase in M4.5+ activity at Parkfield.

data at Parkfield. To map the Cluster Signature throughout the San Andreas system in central California, we used the NCSN (surface sensors) waveforms and catalog for events recorded at Parkfield and compared these results to the higher-resolution picture from the borehole network to calibrate the NCSN sensitivity. We then apply the method to characterize the central San Andreas and Bay Area faults using the more broadly distributed NCSN. The NCSN-determined Cluster Signature is sufficient to characterize some important aspects of waveform similarity and clustering in the fault zone and it shows distinct differences in the seismic signature of these zones both in the degree of hierarchical clustering and in the proportion of clustered earthquakes. These differences imply that potentially useful information on the variable character of California faults can be detected and related to features indicative of fault stress such as hierarchical clustering using the Cluster Signature approach.

6.2 Fault-zone Guided Waves

There has been a lot made of so-called fault-zone guided waves (FZGW). Much of it has been directed toward modeling wave propagation in relatively simple, vertical low-velocity structures in order to match discrete observations of the late, low frequency arrivals sometimes recorded near the fault trace. We have begun to explore this problem from a somewhat different approach, using the extensive observations of these waves in the Parkfield network, the 3-D P- and S-velocity model for the fault zone, and our Vibroseis results that place an apparent strain-related zone of changing wave propagation parameters within the shallow (the upper 3 km) part of the fault zone. In this two-fold investigation we have begun to characterize the distribution throughout the fault zone of source-receiver paths that produce strong FZGW signals from earthquakes. The goal of this part of our research is to be able to first determine the patterns of generation and propagation of FZGW, to characterize the wavefield in terms of velocity and particle motion relative to the fault zone, and finally, to model the phenomenon numerically using new 3-D guided- wave algorithms under development. Our initial work on this is suggesting that the strong generation as well as the wave propagation is a shallow feature of the fault zone. We would like to take this study farther as part of our ongoing Parkfield research plan.

6.3 Current Emphases

The current emphases in the Parkfield project can be illustrated with excerpts from several recent papers:

- Nadeau and McEvilly (1999) devised a method for estimating fault slip rate "... recurring highly similar microearthquakes at Parkfield, California provide a means for inferring slip rate throughout the active fault surface from the time intervals between sequence events. ...an 11-year high-resolution microseismicity record revealed systematic spatial and temporal changes in the slip rate that were synchronous with earthquake activity and other independent indicators of fault-zone slip", Figure 10.12, which provide "...the basis for a new method to monitor the changing strain field throughout the seismogenic fault zone, adding the depth dimension to conventional surface-constrained measurements of deformation."

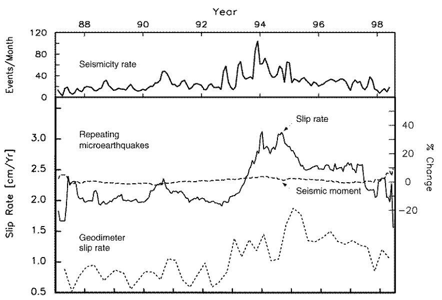

Figure 10.12: (Top) Seismicity rate smoothed with a 2-month running window. (Center) Variations in recurrence-derived slip rate (solid) and sequence-normalized seismic moment (dashed) for 160 repeating microearthquake sequences at Parkfield, CA. The left scale is absolute slip rate, and the right scale is relative change in slip rate and moment. (Bottom) Surface measured slip rate from the two-color laser geodimeter (Langbein et al., in press) at Parkfield

- Korneev et al. (1999) provide a quantitative model of the Vibroseis travel-time anomaly: "... one element of the Parkfield, CA Prediction Experiment, the borehole seismographic network there was illuminated routinely by a large shear-wave Vibroseis from several source points... Clear and progressive travel-time changes of up to 50 msec were detected, most prominent in the S-wave coda, and localized to propagation paths through the fault zone southeast of Middle Mountain, the section of the fault where previous M6 earthquakes have initiated. We model the observations successfully as interaction (reflection and transmission) of the shallow wavefield with a 200-meter-wide low-velocity fault zone in which the velocity increases by 6% due, we hypothesize, to hydrological changes accompanying a significant pulse in slip rate and seismicity."

- Ellsworth et al. (1999), propose a new approach to earthquake probabilities: " A physically-motivated model for earthquake recurrence based on the Brownian relaxation oscillator is introduced. ..... Application of this model to the next M 6 earthquake on the San Andreas fault at Parkfield, California suggests that the annual probability of the earthquake is between 1:10 and 1:13."

- Sammis et al. (1999) use the Parkfield data in developing a fractal asperity model: "...Nadeau and Johnson [1998] found that the smallest events occurred on patches having a linear dimension of the order of 0.5 m, displacements of about 2 cm, and stress drops of the order of 2000 MPa, roughly 10 times larger than rock strengths measured in the laboratory. ... A hierarchical fractal asperity model is presented, which is based on recent laboratory observations of contact distributions in sliding friction experiments. ... The spatial distribution of hypocenters in the Parkfield area is shown to be consistent with this simple fractal model and with a hierarchical clustering of asperities having a fractal dimension of D = 1 and discrete resealing factor of about 20."

- Wenk et al. (1999) see evidence in psuedotachylites for faulting processes inferred from Parkfield microearthquakes: "...The pseudotachylites formed during a late brittle event (56-62 My) and postdated the large ductile mylonitic deformation in the Santa Rosa mylonite zone (65-87 My) as ascertained by 4OAr/39Ar ages. ... From the sizes, energies required for melting estimated to range between 105 J for smaller veins and 1010 J for larger ones. Interestingly the energy distribution and geometry of these pseudotachylites corresponds closely to energy distributions of current microseismic events along the San Andreas fault at Parkfield, suggesting that basic mechanisms may be similar and due to intrinsic mechanical properties of rocks."

6.4 References

Nadeau, R.M. and T.V. McEvilly , Fault slip rates at depth from recurrence intervals of repeating microearthquakes, Science, 285, 718- 721, 1999.

Korneev, V.A., T.V. McEvilly and E.D. Karageorgi, Seismological Studies at Parkfield VIII: Modeling the Observed Controlled-Source Waveform Changes, Bull. Seism. Soc. Am. (submitted), 1999.

Ellsworth, Matthews, Nadeau, Nishenko, Reasenberg and Simpson, A Physically- Based Earthquake Recurrence Model for Estimation of Long-Term Earthquake Probabilities, Geoph. Res. L. (submitted), 1999.

Wenk, H-R., L.R. Johnson and L. Ratschbacher, A Large Psuedotachalyte Zone in the Eastern Peninsular Ranges of California, Tectonophysics (submitted), 1999.

Sammis, C.G.,R.M. Nadeau and L.R. Johnson, How strong is an Asperity, J. Geoph. Res., 104, 10609-10619, 1999.

Langbein, J.O., R. Gwyther, R. Hart, M.T. Gladwin, Slip rate increase at Parkfield in 1993 Detected by High-Precision EDM and Borehole Tensor Strainmeters, Geo-Phys. Res. Lett., in press

7. Hayward Fault Studies

T. V. McEvilly, R. A. Uhrhammer, R. Burgmann, R. M. Nadeau, and R. W. Clymer; BSL, P. Hipley; Caltrans, L. Hutchings; LLNL

7.1 Introduction

The Hayward fault along the eastern side of San Francisco Bay is arguably one of the most hazardous faults in the world when one considers the probability of an earthquake together with the density and nature of development along it. The M~7 October 21, 1868 Hayward fault earthquake produced a 30-to-40-km-long surface rupture, and slip of up to 2 m may have extended at depth from Warm Springs to near Berkeley [Yu and Segall, 1996]. No other large historic earthquake has been unequivocally assigned to the Hayward fault. An 1836 earthquake, long assumed to have ruptured the northern Hayward fault, may actually have occurred on the San Andreas fault to the southwest, implying that the northernmost Hayward fault has not ruptured for at least 160 or perhaps even 220 years [Toppozada and Borchardt, 1998]. Williams [1992] documents at least six Hayward fault ruptures during the past 2100 years in a trenching study on the southern Hayward fault.

Long-term Hayward fault slip rate estimates of ~10 mm/yr. suggest that more than a meter of slip potential has accumulated since the most recent events, making the Hayward fault capable of M≥6.5 events in the near future [Lienkaemper et al., 1991; Savage and Lisowski, 1992]. Accordingly, the Hayward fault has been assigned the highest probability for a destructive earthquake in the Bay area in next 30 years with an estimated recurrence interval of 167±67 years [(WGCEP), 1990]. Estimated 30-year probabilities are 28% for the northern Hayward fault segment, and 23% for the southern part. Estimated cost and loss of life from such an event approach 10's of billions dollars and several thousand deaths, respectively. It is an extremely threatening fault, demanding a better understanding of its pathology. At present we know essentially nothing about its segmentation, and only that it creeps along much of its trace. Initial steps have been taken in modernizing the seismographic and geodetic instrumentation along the fault zone, and this project will use these accumulating data in new ways to better define the deformation in space and time.

7.2 Hayward Fault Seismicity

We have initiated the computationally intensive search for characteristic sequences on the Hayward fault, where seismicity resembles the Parkfield clustering, at a lower rate. The initial processing defines the 'Clustering Signature' (CS) for the seismicity on any seismogenic fault segment, and this signature reveals the pathology of that fault in terms of waveform similarity within the population of events, a unique characteristic of the fault zone that defines the degree of clustering in the earthquake process. In Figure 10.13 we illustrate CS with three examples calculated with waveforms from NCSN stations at Parkfield and at two places on the Hayward fault. Even at reduced detection completeness (M~1.3) of NCSN without the borehole network data, we see highly similar events (coherency ≥ 0.5) in the NCSN catalog. Seismicity on the Hayward fault resembles the 'clusters of clusters' pattern seen at Parkfield.

The fraction of total seismicity made up by the repeating events on a fault segment is proportional to the slip rate in the model of Nadeau and McEvilly (1999), and the data support the model. The fractions are 48%, 13% and 6%, respectively, for Parkfield, southern Hayward/Mission and northern Hayward fault segments, within the NCSN catalog. If the data base from the borehole network at Parkfield (detection threshold M_L 0) is used to determine the fraction, it is about 67%. At Parkfield, where fault slip is around 25 mm/yr, the recurrence time for M_L~0.0 is 3 to 6 months. Scaling to 10 mm/yr on the Hayward fault yields a value of 7 to 15 months repeat times. For the borehole stations, the improved signal-to-noise ratios being attained are pushing down the detection threshold to somewhere between M_L 0.0 and M_L -0.6 for local events. The expected rate of seismicity within a 10 km radius of Berkeley is 3 per month at M_L 0.0 or 10 per month at the M_L -0.6. We conclude that adequate data are expected to be available for this exercise from the Hayward fault borehole network, accessible from the optical mass-store archive at NCEDC. Our early search is identifying sequences of repeating events consistent with our expectations.

7.3 Slip Rate from Earthquake Recurrence

This method has recently been developed in our research program using data from another borehole network along an active fault zone. Studies at very high resolution of microearthquakes at Parkfield, CA since 1987

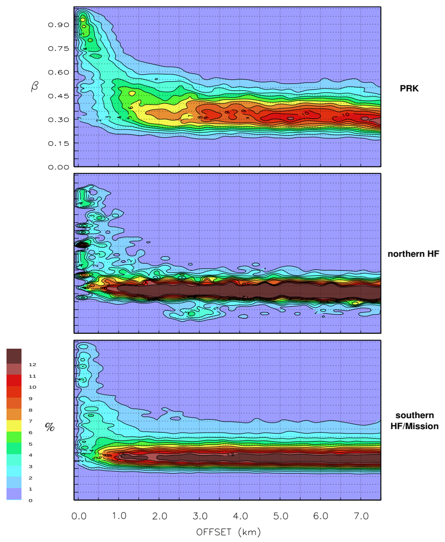

Figure 10.13: Cluster Signatures from NCSN waveform archives for earthquakes at Parkfield (PRK), the northern Hayward Fault (northern HF), and southern Hayward / Mission faults (southern HF/Mission). In this analysis, comparisons of waveform similarity between all possible pairs of earthquakes are made. The similarity of the earthquakes, as manifest in maximum waveform cross-correlations, are shown on the ordinate (β) axis and the distance between the two events is given on the abscissa. Contoured values show the relative number of event pairs with given similarity separated by a given distance. Hence spatial clusters of very similar earthquakes (including all repeating earthquakes) plot in the upper left hand quadrant, while less similar widely separated earthquake pairs plot in the lower right hand quadrant. Note that theoretically for completely uncorrelated waveforms, β should be equivalent to the maximum correlation of white noise (ie. 0.25).

revealed a systematic organization in space and time, dominated by clustering of nearly identical, regularly occurring microearthquakes ('characteristic events') on 10-20 m wide patches within the fault zone (Nadeau and McEvilly, 1997, 1999). At Parkfield, more than half of the 5000+ events in the 1987-1998 catalog exhibit this trait. In general, recurrence intervals (0.5 to 2 yr.) scale with the magnitude of the repeating events for the magnitude range available (M_w 0.2 to 1.3). Clusters of these characteristic events occur throughout the slipping fault surface. Scalar seismic moments were estimated for 53 of the repeating sequences and combined with equivalent estimates from 8 similar but larger event sequences from the Stone Canyon section of the fault and the main Parkfield M6 sequence. These estimates show that seismic moment is being released as a function of time in a very regular manner. Measurements of the moment release rate, combined with an assumed tectonic loading rate, lead to estimates of the seismic parameters source area, slip, and recurrence interval. Such parameters exhibit a systematic dependence upon source size over a range of 10^{10} in seismic moment which can be described by simple scaling relationships (Nadeau and Johnson, 1998). What emerges from this analysis of moment release rates is a quantitative description of an earthquake process that is controlled by small strong asperities that occupy less than 1% of the fault area. A 26-months period of greatly increased activity during the study interval (M4.2, 4.6, 4.7 and 5.0 events and their aftershocks) accompanied changes up to 50% in previously stable recurrence intervals. Langbein et al. (1998) report on evidence in deformation measurements for a slip rate increase in 1993 at Parkfield. Nadeau and McEvilly (1999) show that it is possible under reasonable assumptions to infer the spatial distribution of variations in slip-rate on the fault surface from the changes in recurrence intervals for the characteristic event sequences. The analysis requires an assumption of constant area for the repeating sources - one easily supported by the lack of any detectable change in the waveforms (over the 100 Hz bandwidth) associated with the change in recurrence interval.

7.4 Improving Inversion for Fault Slip

We model the measured displacement field with rectangular displacement discontinuities with uniform slip in an homogeneous elastic half-space. A number of modeling and inversion tools have been developed that will enhance our ability to model these new data [e.g., Murray et al., 1993, 1996; Burgmann et al., 1994; 1997]. The addition of subsurface slip constraints to the inversion is fundamental to this proposed study. Even with the InSAR-quality range-change data available crossing the Hayward fault, determination of the vertical extent (creep patch width) of the creeping zone is nearly impossible to recover if the locked zone is deeper than about 3 km. Slip distribution at depth is elusive, and asperities are cannot be imaged even near the surface, without subsurface slip information. The next M6.5+ event on the Hayward fault will likely nucleate typically near the lower bound of the seismogenic zone, a depth of 8-10 km, where resolution of the slip distribution from surface observations is very poor. Constraints from recurrence-determined slip rates at a few depth points offers promise for substantially sharpened resolution near the all-important base of the slipping zone. We are working to improve the slip inversion data set by adding to the growing InSAR data base a combination of microearthquake-determined slip rates throughout the fault zone and enhanced GPS coverage from a tight rotating deployment of single-frequency L1 receivers in the center of our study region.

7.5 The M_w 4.1 El Cerrito Earthquake

The largest local earthquake that occurred along the northern segment of the Hayward Fault during the past year was a M_w 4.1 event which occurred at 4:16 AM local time on December 4, 1998 at a depth of 6.8 km along the Hayward Fault approximately 6.3 km northwest of the Berkeley campus. This earthquake was recorded by all the northern Hayward Fault Network stations and by the Caltrans bridge borehole sites.

Ground motions recorded at BDSN stations in the vicinity of the northern Hayward Fault are shown in Figure 10.14. The relative ground velocity traces are ordered from top to bottom by epicentral distance. Note the variation in the seismic wavefield with distance, azimuth, and side of the Hayward Fault. The crustal structure across the northern Hayward Fault zone, in the vicinity of Berkeley, is rather complex with a lateral bedrock velocity contrast of approximately 30% across the fault zone with the SW side fast and also with an attenuation contrast across the fault zone with the NE side having higher attenuation as evidenced by the variability in the observed seismic ground motions shown in Figure 10.14. For example, the observed waveforms at BKS (6.8 km away on NE side) and at BRK (5.8 km away on SW side) show considerable variation in the high-frequency spectral content, in the low-frequency coda duration, and in the S-P interval (a 60% change for a 20% increase in distance. The observation that the first motions at BKS and BRK are both dilational is an indication, given the right-lateral strike-slip source mechanism and compressional quadrant path to BKS, that the initial P-wave recorded at BKS is laterally refracted along the fault zone.

Bedrock ground motions at seven locations along the Bay Bridge for the M_w 4.1 earthquake are shown in Figure 10.15. Note that the character and phasing of the ground motion varies considerably from east to west (top to bottom in Figure 10.15) as the wavefield propagates across San Francisco Bay. Knowledge of the bedrock ground motions is of paramount engineering importance for seismic design of the bridge.

7.6 References

(WGCEP), W.G.C.E.P., Probability of large earthquakes in the San Francisco Bay Region, California, U.S. Geol. Surv. Circ., 1053, 1-51, 1990.

Burgmann, R., R. Arrowsmith, T. Dumitru, and R. McLaughlin, Rise and fall of the southern Santa Cruz Mountains, California, deduced from fission track dating, geomorphic analysis, and geodetic data, J. Geophys. Res., 99 (B10), 20181-20202, 1994.

Burgmann, R., P. Segall, M. Lisowski, and J. Svarc, Postseismic strain following the 1989 Loma Prieta earthquake from GPS and leveling measurements, J. Geophys. Res., 102, 4933- 4955, 1997.

Langbein, J., R.L. Gwyther and M.T. Gladwin, Possible increase in fault slip rate at Parkfield in 1993 as inferred from deformation measurements from 1986 to 1997, Seism. Res. L., 69, 151, 1998.

Lienkaemper, J.J., J.S. Galehouse, and R.W. Simpson, Creep response of the Hayward fault to stress changes caused by the Loma Prieta earthquake, Science, 276, 2014-2016, 1997.

Murray, M.H., J.C. Savage, M. Lisowski, and W.K. Gross, Coseismic displacements: 1992 Landers, California, earthquake, Geophys. Res. Lett., 20, 623626, 1993.

Murray, M. H., Marshall, G. A., Lisowski, M., and Stein, R. S., The 1992 M=7 Cape Mendocino, California, earthquake: Coseismic deformation at the south end of the Cascadia megathrust,

Nadeau, R. M. and L. R. Johnson, Seismological Studies at Parkfield VI: Moment Release Rates and Estimates of Source Parameters for Small Repeating Earthquakes, Bull. Seism. Soc. Am.,. 88, 790-814, 1998.

Nadeau, R.M. and T.V. McEvilly , Fault slip rates at depth from recurrence intervals of repeating microearthquakes, Science (submitted), 1999.

Savage, J.C., and M. Lisowski, Inferred depth of creep on the Hayward fault, central California, J. Geophys. Res., 98, 787-795, 1992.

Toppozada, T.R., and G. Borchardt, Re-evaluation of the 1836 "Hayward fault" and the 1838 San Andreas fault earthquakes, Bull. Seism. Soc. Am., 88, 140-159, 1998.

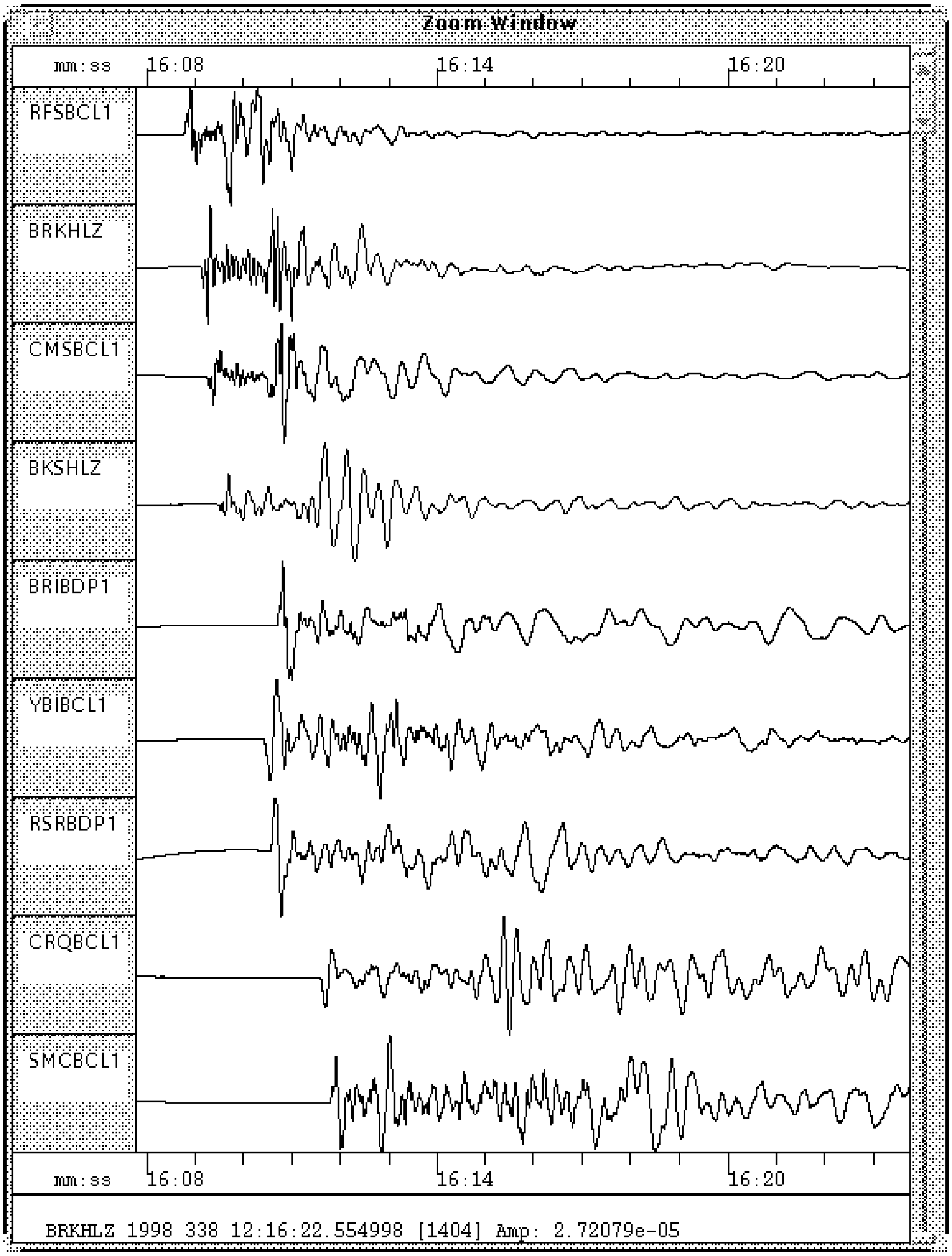

Figure 10.14: Ground motions at nine locations in the vicinity of the northern Hayward fault for the 12/04/98 Hayward Fault earthquake. The traces are vertical-component relative ground velocities and they are ordered top to bottom by epicentral distance. All stations are in boreholes except for SMCB which is in a 4 m posthole and BKS and BRK which are standard BDSN broadband stations in surface vaults.

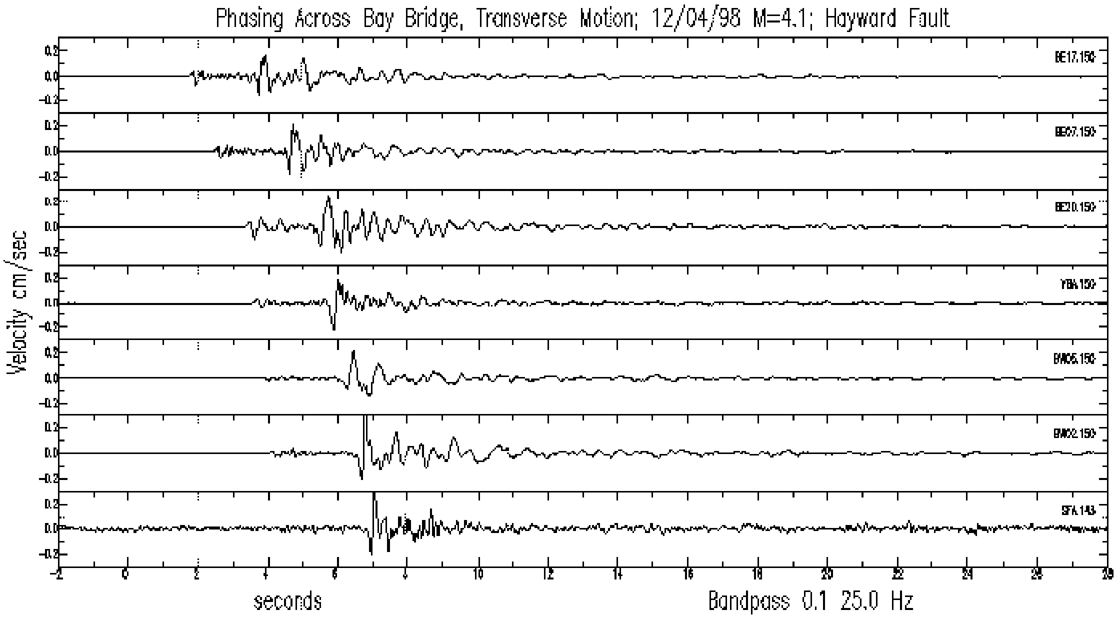

Figure 10.15: Ground motions at seven locations in bedrock along the Bay Bridge from the M_w 4.1 earthquake located on the northern Hayward Fault approximately 13 km NNE of Yerba Buena Island (the middle trace). Velocity records transverse to the bridge are shown and all traces are to the same scale.

Williams, P.L., Geologic record of southern Hayward fault earthquakes, Div. Mines Geol. Spec. Pub., 113, 171-179, 1992.

Yu, E., and P. Segall, Slip in the 1868 Hayward earthquake from the analysis of historical triangulation data, J. Geophys. Res., 101 (B7), 16,101-16,118, 1996.

8. Inversions for buried slip along the northern Hayward fault from GPS and InSAR data

Roland Bürgmann, Eric Fielding, Mark Murray, David Schmidt

8.1 Introduction

On October 21, 1868, the only major historic earthquake on the Hayward fault produced a 30-40-km-long surface rupture with slip of up to 2 m which may have extended at depth from Fremont to as far north as Berkeley. No large historic earthquake has been unequivocally attributed to the Hayward fault north of this rupture, suggesting a lack of coseismic rupture since before the establishment of the first Spanish mission in the region, in 1776 (*Toppozada and Borchardt* 1998). A paleoseismic trenching investigation on the northern Hayward fault suggests an earthquake rupture after 1640 AD (*Schwartz et al.* 1998, pers. comm.). Long-term slip rate estimates of 10 mm/yr indicate that more than 2 m of seismic slip potential has accumulated since the most recent event, making the northern Hayward fault capable of M > 6.5 events.

Earthquake potential estimates are complicated by the occurrence of shallow aseismic creep along the Hayward fault whose depth extent is not known. At the surface, the Hayward fault creeps at 3-9 mm/yr (*Lienkaemper et al.,* 1997). It is not clear over what depths locked and creeping portions of the Hayward fault extend, leading to substantial uncertainty about potential earthquake magnitudes and probabilities.

Measurements of surface displacements surrounding a fault using GPS or terrestrial surveys can be used to compute models of the distribution of slip on a fault system. However, most precisely surveyed points near the Hayward fault are spaced more than 10 km apart and it is therefore difficult to determine a reliable slip estimate. Space based Interferometric Synthetic Aperture Radar (InSAR) can map ground deformation at 10s-of-meter resolution over large areas with sub-cm precision. This technique only provides measurements of one component of the displacement field along the look direction of the radar. The Global Positioning Systems (GPS) can measure the three-dimensional displacements at very high precision, but station spacing currently are limited to several km. We utilize surface creep rates established over several decades (*Lienkaemper et al.,* 1997), GPS measurements spanning about 4 years, and InSAR data spanning a 5-year period from June 1992 to September 1997 (Figure 10.16), to invert for the depth of creep on the northern Hayward fault.

8.2 Results

Measurements of active deformation along the northern Hayward fault consist of surface creep data at the active fault trace, GPS measurements of benchmark motions, and InSAR measurements of range change differences near the Hayward fault. We assume that the deformation has been steady and integrate creep rates from the last several decades with GPS derived displacements between 1993 and 1998, and InSAR measured range changes between 1992 and 1997.

Along the northern 15 km of the subaerial portion of the Hayward fault, surface creep rate estimates average 5-6 mm/yr (*Lienkaemper et al.,* 1997). GPS station velocities along the northern Hayward fault are from continuously operating receivers of the BARD (Bay Area Regional Deformation) network, as well as from campaign style measurements collected since 1993 by the U.S. Geological Survey and the University of California, Berkeley.

We use synthetic aperture radar (SAR) data collected by the European Space Agency (ESA) ERS-1 space craft on June 10, 1992 and September 06, 1997. Bürgmann et al. (1998) utilized a 1992-1995 image pair to examine anomalous slip patterns along the southern Hayward fault resulting from the effects of the 1989 Loma Prieta earthquake. Discrete offsets due to aseismic creep at the surface are apparent along the trace of the actively creeping Hayward fault. This suggests a component of surface fault displacement in the satellite range direction. InSAR only measures the motion as it projects into the satellite range direction which is 23 degrees off vertical for ERS.

We use elastic dislocation models to estimate the distribution of locked and slipping portions of the Hayward fault. For the purpose of this study, we assume that the northern Hayward fault northwest of Berkeley is characterized by uniform creep from the surface to some depth. Regional interseismic strain accumulation across the San Andreas fault system is represented by slip on deeply buried dislocations below the San Andreas and Hayward fault zones. The regional model is formally derived from the GPS data, which are well fit by the model.

Integration of the range change data with sparse, but precise GPS measurements in the region helps us bet-

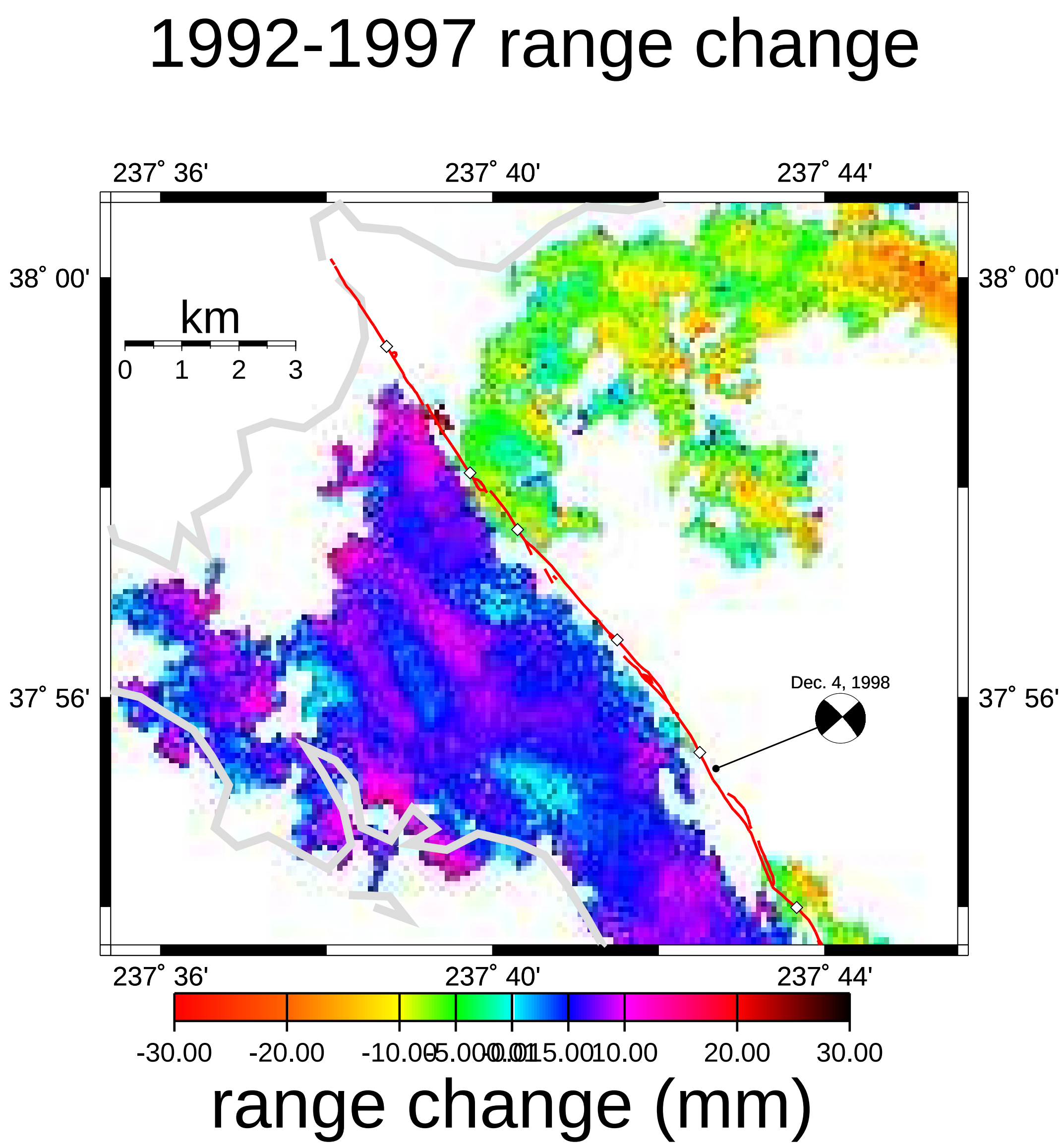

Figure 10.16: Unwrapped interferogram of two ERS images spanning 5.25-year period of faulting and strain accumulation near Hayward fault (ERS track 70, frames 2835 and 2853; June 10, 1992, ERS-1 orbit 4724, and September 06, 1997, ERS-2 orbit 12449). Range changes are computed from InSAR interferogram by unwrapping angular phase delays and converting from phase delay to range change. Steep topography and heavy vegetation cause decorrelation leading to loss of range change information (blank areas). Good correlation occurs almost exclusively in urban areas. An abrupt offset follows trace of recently active strands of Hayward fault indicated by thin red line.

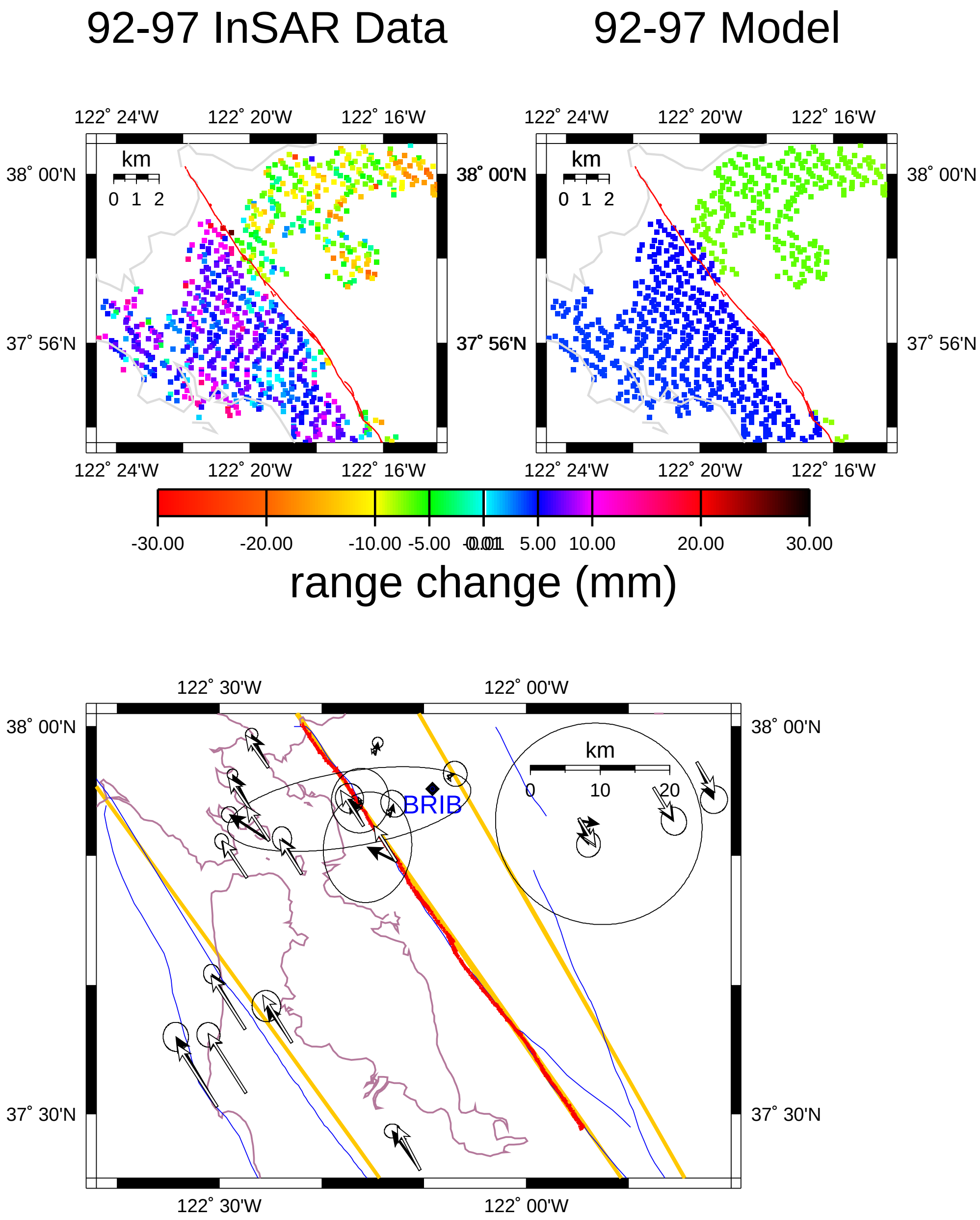

Figure 10.17: Joint inversion of GPS and InSAR data. We can now formally combine the two data sets in our model inversions. Preliminary results using the existing GPS data set shown in the bottom panel (solid arrows) and 1992-1997 InSAR data shown in the top left panel (subsampled to the number of data points shown) suggest a best fitting model with creep to 7 km. Additional GPS data and additional redundant InSAR data are required to better constrain our models.